Please do not adjust margins

CrystEngComm

ARTICLE

$K_2Mn^{II}_2(H_2O)_2C_2O_4(HPO_3)_2$: A New 2D Manganese(II) Oxalatophosphite with Double-Layered Honeycomb Sheets Stabilized by Potassium Ions

Received 00th January 20xx,
Accepted 00th January 20xx

DOI: 10.1039/x0xx00000x

www.rsc.org/

Joseba Orive,[a]* Ramesh Sivasamy,[a] Roberto Fernández de Luis,[b,c] Edgar Mosquera[d] and María I. Arriortua[b,c]

A novel 2D metal oxalatophosphite $K_2Mn^{II}_2(H_2O)_2C_2O_4(HPO_3)_2$ (**KMnCP**) was hydrothermally synthesized and characterized. The hexagonal morphology and crystal growth faces of **KMnCP** were predicted by Bravais–Friedel–Donnay–Harker (BFDH) theory. Single crystal X-ray diffraction analysis revealed that the compound displays a unique double layered structure constructed from $Mn(H_2O)(HPO_3)$ single layers linked by oxalate ligands, where the potassium levels interrupt the 3D connectivity through the organic bridges. Moreover, in order to classify this archetype a crystallochemical revision of the metal oxalatophoshites with anionic frameworks has been carried out. Several Secondary Building Units (SBUs) formed by metal-phosphite substructures and different roles of de oxalate bridges have been observed, what has led to propose a new structural classification for this kind of materials with common features between the classic inorganic metal phosphates and coordination polymers. Finally, the thermal, spectroscopic and magnetic properties together with the electronic structure of the studied compound are discussed.

Introduction

The design of new sophisticated hybrid materials containing inorganic and organic linkers has experienced a clear interest reflected mainly in the development of a huge number of multifunctional metal–organic frameworks (MOFs) with applications in several fields.[1] The reticular chemistry approach applied during the last decade to synthesize MOFs can be translated to obtaining other inorganic-organic compounds containing a mixture of carboxylate based linkers and inorganic anions, such as phosphate, vanadate or arsenate groups, just to mention some of them.[2] One of these classes of hybrid frameworks is based on oxalate and phosphate groups in which the metal centers are coordinated by both types of ligands, giving rise to extended structures containing common features with the classic inorganic metal phosphates and coordination polymers. As in inorganic-organic classic metal phosphates, many of these called transition metal oxalatophosphates have been prepared using organic templates giving rise to crystalline materials with channels similar to those found in zeolites.[3] Inorganic and organic templates act as structural directing agents, located at the pores of the structure, and balancing the negative charge of the inorganic skeleton.

Unlike classical 4-coordinated PO_4 units, HPO_3 characteristics such as a reduced charge and a fewer number of P-O binding sites can be exploited to design different connectivity patterns.[4] In this sense, many successful examples of organically templated oxalatophosphites including different metals such as indium,[5] cobalt,[6] manganese,[7] iron,[8] gallium[9] and lanthanides[10] have been reported during the last decade.

In contrast to the organically templated zeotypes, examples of oxalate- phosphates[11] and phosphites[12] with alkali metal charge compensating cations as inorganic templating agents encapsulated into the metal organic-phosphate frameworks are scarcer. Due to their similitudes with the coordination polymers, M. Nagarathinam et al.[13] defined these inorganic-organic materials as metal organic–phosphate open frameworks (MOPOFs). Such hybrid materials were tested as cathode materials for lithium ion batteries (LIBs), demonstrating to have great feasibility of exchanging K^+ with Li^+ ions and showing good capacity of reversible lithium insertion/extraction.[14] Despite the insertion of the organic

[a] Departamento de Ciencia de los Materiales, FCFM, Universidad de Chile, Av. Beauchef 851, Santiago 8370448, Chile. E-mail: joseba.orive@ing.uchile.cl; Fax: +56 2269 94119; Tel: +56 2297 71076.
[b] Departamento de Mineralogía y Petrología, Facultad de Ciencia y Tecnología, Universidad del País Vasco (UPV/EHU), Apdo. 644, 48080 Bilbao, Spain. E-mail: roberto.fernandez@ehu.es, maribel.arriortua@ehu.es; Fax:+34 946 013 500; Tel: +34 946 015 984.
[c] Basque Center for Materials, Applications & Nanostructures (BC Materials) Parque Tecnológico de Zamudio, Camino de Ibaizabal, Edificio 500 - 1º, 48160 Derio, Spain. E-mail: roberto.fernandez@bcmaterials.net, maribel.arriortua@ehu.es; Tel: +34 946 128 811.
[d] Departamento de Física, Universidad del Valle, A.A. 25360, Cali, Colombia; E-mail: edgar.mosquera@correounivalle.edu.co; Fax:+57 2 3393237; Tel: +57 2 3394610.

Electronic Supplementary Information (ESI) available: [Powder X-ray diffraction pattern matching analysis, intra-layer hydrogen bonds scheme, coordination environment of K(1) atoms, topological representation of VOHMUC, growth model of the crystal, structural visualization of the analysed metal oxalatophosphites, thermal analysis (TGA, DSC) and thermodiffractogram, IR and Raman spectra comparison, UV-Vis spectrum, calculated band structure (TDOS and PDOS), temperature dependence of χ_m and $1/\chi_m$ and magnetic data fitting of **KMnCP**]. See DOI: 10.1039/x0xx00000x

This journal is © The Royal Society of Chemistry 20xx

Please do not adjust margins

Please do not adjust margins

ligand in the hybrid materials decreases the specific capacity of the cathodes, on the other hand it opens new frontiers to explore the lithium ion reversible exchange and migration within more flexible designs of inorganic-organic two-dimensional materials. The phosphate replacement by phosphite units gave rise to obtaining a new family of redox active vanadyl oxalatophosphites with $A_2[(VO)_2(HPO_3)_2(C_2O_4)]$ (A = Li, Na and K) formula.[12b] This approach has the advantage of getting similar archetypes to that found in the previous mentioned oxalatophosphates together with the increase of the theoretical specific capacity of the compounds due to decrease in the molecular weight.

Such achievements encourage the search of new hybrid materials by varying the alkali and transition metal, organic ligands, or polyanion units which could lead to better and rentable cathode materials with new architectures.

As part of our pursuit of new host lattices with redox-active metal centers which are able to encapsulate mobile ions, here we disclose an experimental and theoretical study of the first manganese (II) oxalatophosphite with an alkali metal charge compensating cation which presents a not very usual layered topology. Moreover, a new structural classification for metal oxalatophosphites has been formulated taking into account the dimensionality of the inorganic metal phosphite skeleton and the role of the oxalate in the structures.

Experimental section

Synthesis and characterization

$K_2Mn^{II}_2(H_2O)_2C_2O_4(HPO_3)_2$ (**KMnCP**) was prepared using mild hydrothermal conditions under autogenous pressure. A mixture of H_3PO_3 (7.5 mmol), $MnCl_2{\cdot}4H_2O$ (0.75 mmol) and $C_2K_2O_4{\cdot}H_2O$ (1.5 mmol), was dissolved in distilled water (25 ml) and stirred in air. Then, around 5.4 ml of 2M KOH solution was added dropwise to increased up the pH of the resulting solution to 5.0. The reaction mixture was sealed in a 50 ml PTFE-lined stainless steel pressure vessel (fill factor 65%). After 3 days at 120 °C, large hexagonal plates and prismatic crystals of **KMnCP**, suitable for single crystal X-ray diffraction, were recovered and washed with water and acetone. Some unidentified acicular crystals were removed by decantation from the final product. Fine white powder as pure phase of **KMnCP**, for further characterization, was achieved by decreasing the heat treatment temperature to 100 ºC.

Another possible mobile ions, such as lithium and sodium were tried to encapsulate in the system, but $A_x(H_3O)_{2-x}Mn_5(HPO_3)_6$ (A = Li, Na) inorganic phosphites crystallize[15] (Fig. S1).

The manganese, phosphorous and potassium contents were confirmed by inductively coupled plasma quadrupole mass spectrometry (ICP-Q-MS) analysis, performed with a Thermo Scientific XSERIES 2 spectrometer. The amount of C was calculated by elemental analysis. $K_2Mn_2(H_2O)_2C_2O_4(HPO_3)_2$ (**KMnCP**). Calc: K, 16.56; Mn, 23.27; P: 13.12; C, 5.09; H, 1.28. Found: K, 13.5(4); Mn, 23.4(5); P: 12.7(5); C, 4.5(4); H, 1.6(2). The density of the compound as single crystal was measured by flotation[16] using a mixture of bromoform and bromobenzene, being 2.53(4) $g.cm^{-3}$.

Single crystal X-ray diffraction study

A hexagonal prism with dimensions 0.269 x 0.083 x 0.073 mm of the studied compound was selected under a polarizing microscope and glued on a glass fiber. Intensity data were collected at 100 K on an AGILENT SUPERNOVA single source diffractometer with Mo Kα radiation using a CCD (Eos) detector. Data frames were processed (unit cell determination, intensity data integration, correction for Lorentz and polarization effects,[17] and analytical absorption correction[18] taking into account the size and shape of the crystal) using the corresponding diffractometer software package.[19] The structure was solved by direct methods, SHELXS 97 computer program,[20] in the hexagonal space group $P6_3/m$, and then refined by the full matrix least-squares procedure based on F^2, using the SHELXL 97 computer program[21] belonging to the WINGX software package.[22] TWINROTMAT option of PLATON program[23] suggested the existence of a merohedric twin by 180º rotation around the [120] reciprocal lattice direction, in agreement with the twin's law expressed by the [-100, 110, 00-1] matrix. After the refinement, the masses of the two components of the twin were found to have percentages of 58.9(2) and 41.1(2).

This scheme permitted us to find the positions of the manganese and phosphorous atoms, and all the other non-hydrogen atoms (K, O and C) were placed from subsequent Fourier-difference map calculations. Next, the hydrogen atoms related to the phosphite units were located. Finally, the hydrogen atoms related to the coordinated water molecule were first located and placed in geometrically ideal positions (O–H: 0.82(1) Å; H–H: 1.35(2) Å) and refined using the riding model. The atomic displacement parameters (ADPs) for all atoms except hydrogens were described using an anisotropic model.

Details of crystal data measurement and reduction, structure solution and refinement of **KMnCP** are reported in Table 1. The selected bond distances and angles are reported in ESI, Table S1. Structure drawings were made using the ATOMS 6.2.[24]

Powder X-ray diffraction

X-ray powder diffraction measurement for qualitative phase analysis using the pattern matching routine of the FULLPROF program[25] for **KMnCP** was recorded at room temperature using a PHILIPS X'PERT PRO automatic diffractometer equipped with Cu Kα radiation source (λ = 1.5418 Å). The power generator was set to 40 kV and 40 mA and the pattern was recorded in 2θ steps of 0.026° in the range of 5-70°. The systematic 2θ shift; peak shape (pseudo-Voigt), U, V, and W half-width parameters for the profile function, the previously obtained unit cell parameters, asymmetry parameters, and the background were refined. Starting from the space group and the lattice constants of the compound previously studied by single crystal X-ray diffraction, we reached to good agreement between the

 This journal is © The Royal Society of Chemistry 20xx

Please do not adjust margins

Please do not adjust margins

experimental and the calculated diffractograms (Fig. S2). Besides, the inset of Fig. S2 shows the great similarity between the experimental powder pattern and the one simulated from the single crystal X-ray diffraction solution, confirming the phase purity of the as-prepared sample.

Table 1 Crystallographic data and structure refinement parameters for **KMnCP** obtained by single crystal X-ray diffraction

Molecular weight ($gmol^{-1}$)	472.08
Space group	$P6_3/m$
a, c (Å)	9.7371(2), 22.4924(5)
V ($Å^3$), Z	1846.82(7), 6
ρ_{obs}, ρ_{calc} (gcm^{-3})	2.53(4), 2.547
Cristal size (mm)	0.269 x 0.083 x 0.073
F(000)	1392
Diffractometer / Temperature (K)	AGILENT SUPERNOVA (omega scan mode) / 100(2)
μ (mm^{-1}), Tmin./Tmáx.	3.046, 0.542/0.842
Radiation (Å)	λ(Mo Kα) = 0.71073
Limiting indices h, k, l	$h \pm 12$, $-12 \le k \le 10$, $-29 \le l \le 23$
Theta range (°) Completeness (%)	$1.81 \le \theta \le 28.34$, 95.3
N. reflections measured / independents / observed	13563 / 1507 / 1431
R (int) / R(sigma)	0.0383 / 0.0233
Parameters / Restrictions	108 / 3
R [I>2σ(I)]	R1= 0.0241, wR2= 0.0529
R [all data]	R1= 0.0259, wR2= 0.0540
Weight factor	x = 0.0190; y = 1.4895
G. O. F	1.053
Max. and Min. e. density ($eÅ^{-3}$)	0.531, -0.705

Physicochemical characterization techniques

Thermogravimetric analysis was performed under synthetic air on a Netzsch STA 449 F3 Jupiter simultaneous TG-DSC thermo-microbalance. An alumina crucible containing around 15 mg of the sample was heated in air at a rate of 5 °C/min from room temperature to 800 °C. Thermodiffractometric experiment was carried out in air with a Bruker D8 Advance diffractometer (Cu Kα radiation) equipped with, a variable-temperature stage (HTK2000), a Pt sample heater and a Vantec high-speed one dimensional detector with six degrees of angular aperture. The powder patterns were recorded in the $5 \le 2\theta \le 38º$ range (step size = 0.033º and time per step = 0.5 s) at intervals of 15 ºC, increasing the temperature at 10 $ºCmin^{-1}$ from room temperature to 810 ºC. The infrared (IR) spectrum (KBr pellet) was obtained with a JASCO FT/IR-6100 spectrophotometer in the 400-4000 cm^{-1} range, using the KBr pellet technique. Raman spectroscopy was measured on a powdered sample using a Renishaw RM-1000 spectrophotometer equipped with a thermoelectrically cooled charge-coupled device (CCD) detector. A radiation of 785 nm wavelength laser was used to collect Raman spectrum (operating at maximum power, 1 mW power on sample surface). The laser was focused onto the samples using a Leica microscope with a 50× objective lens. Diffuse reflectance spectrum was measured at room temperature using a Varian Cary 5000 spectrophotometer in the 200–2500 nm range. Magnetic measurements on the powdered sample was performed in the temperature range 5.0-250 K, at 0.1 and 0.01 T using a Quantum Design MPMS-7T SQUID magnetometer.

Computational methods

The peripheral morphology and possible crystal growth faces of **KMnCP** crystal have been predicted by Bravais-Friedel-Donnay-Harker (BFDH) method. BFDH is strictly based on the symmetry of the crystal lattice to generate an ordered list of possible growing faces. The relative growth rate of {hkl} forms (G_r) is inversely proportional to the interplanar distance d_{hkl} ($G_r \sim 1/d_{hkl}$). The larger the d_{hkl}, the more pronounced the morphological importance of the face. The electronic structure calculations were executed using DMol3 code of Accelrys package. The calculation is based on density functional theory (DFT) with the plane-wave pseudopotential method. The Perdew-Burke-Ernzerhof (PBE) of generalized gradient approximation (GGA) was used as the exchange-correlation function. A plane wave energy cut-off was set to 300 eV (ultra-soft pseudopotential) and Brillouin-zone integrations were performed using Monkhorst–Pack k-points of 2 × 2 × 1. The criterion of convergence for the residual forces is set to be less than 0.01 eV/Å and the change of total energy less than 5×10^{-6} eV.

Results and discussion

Structure description

The asymmetric unit of **KMnCP** contains 13 non-hydrogen atoms (C, K, Mn, O and P), 3 hydrogen atoms related to the phosphite units and 2 ones associated to a coordinated water molecule (Fig. S3). Mn(1), K(1) and the six oxygen atoms crystallographically independent occupy general positions. The three phosphorous atoms are situated in special positions 4e (P1) and 4f (P(2) and P(3)) with 3.. site symmetry, meanwhile C(1) and C(2) carbon atoms occupy 6h special positions over m.. site.

The structure of **KMnCP** is built of two 2D $Mn(H_2O)(HPO_3)$ single layers linked by oxalate ligands giving rise to 2D anionic double sheets of $[Mn(H_2O)(HPO_3)(C_2O_4)]^{2-}$ formula placed parallel to the ab-plane (Fig. 1a). The distorted $MnO_5(H_2O)$ octahedra are corner-shared with three different $(HPO_3)^{2-}$ units forming a honeycomb hexagonal pattern (Fig. 1b). The coordination sphere of the manganese cations is completed by a terminal aqua ligand and an oxalate unit (Fig. 1c). The double anionic sheets are stacked along the c-direction by K^+ ions giving rise to a 3D structure (Fig. 1a).

In the present structure, it is noteworthy that the oxalate anion as tetradentate ligand bonds to two manganese atoms in bidentate-chelating mode, thus forming the peculiar double anionic sheets (Fig. 1c). The shortest metal-oxygen distances are those which are linked to phosphite units in the ab plane ranging from 2.125(1) Å to 2.161(2) Å. M-O bond lengths increasing up to 2.227(2) Å and 2.237(2) Å are observed for the linkages shared with oxalate units. The longest manganese-

Please do not adjust margins

Please do not adjust margins

oxygen distance (2.245(1) Å) is ascribed to the terminal aqua ligand. All the metal-ligand distances are in good agreement with 2+ oxidation state for the manganese atom, based on the bond valence sums (BVS) calculations.[26] [$Mn(1)O_5(H_2O)$] *cis* angles vary from 73.41(5)º to 99.55(7)º, while *trans* angles values are in the 163.85(6)º-175.92(6)º range. The S(O_h) value, calculated by Continuous Simmetry Measure,[27] is 0.889, near the value for the octahedral ideal symmetry (S(Oh) = 0.00).

The water molecule coordinated to the manganese polyhedron establishes a triangular patterned intralayer H-bonding scheme (Fig. S4). The average bond length distances and angles O-H···O with the oxygen atoms O(4) and O(6) of the oxalate units are ~ 2.67 Å and in the 160-165º range respectively, suggesting a moderate to strong character of the interactions.[28] All P atoms adopt pseudo-pyramidal coordination geometry linking to three Mn atoms via bridging oxygen atoms and to one H atom. The P-O distances are very regular ranging from 1.526(2) to 1.531(2) Å and the P-H distances vary from 1.30(4) to 1.33(4). The O-P-O and H-P-O angles (106.00(7)-112.71(6)º) are in the usual range for phosphite based compounds.[29]

The framework stoichiometry of [$Mn(H_2O)(HPO_3)(C_2O_4)$] creates a net charge of -2, which is balanced by two interlayer potassium ions. So, the potassium counter ions play a predominant role in the stabilization of the three-dimensional network by ionic bonding contacts involving the oxygen atoms of the phosphite moieties and the coordinated water molecule (Table S1, Fig. S5a). The nine-coordinated potassium cations are surrounded by nine neighboring [KO_9] polyhedra, sharing corners with six of them (K-K = 5.497(1)-5.724(1) Å), via one common edge O(1)-O(1) (K-K = 3.606(1) Å) and via two face-shared arrangements (3.640(1) Å). The volume occupied by the K^+ ions was analyzed using the ToposPro 5.0 program[30] by means of Voronoi–Dirichlet polyhedra (VDP)[31], obtaining a value of 270.62 $Å^3$, which supposes the 14.65% of the cell total volume (Fig. S5b).

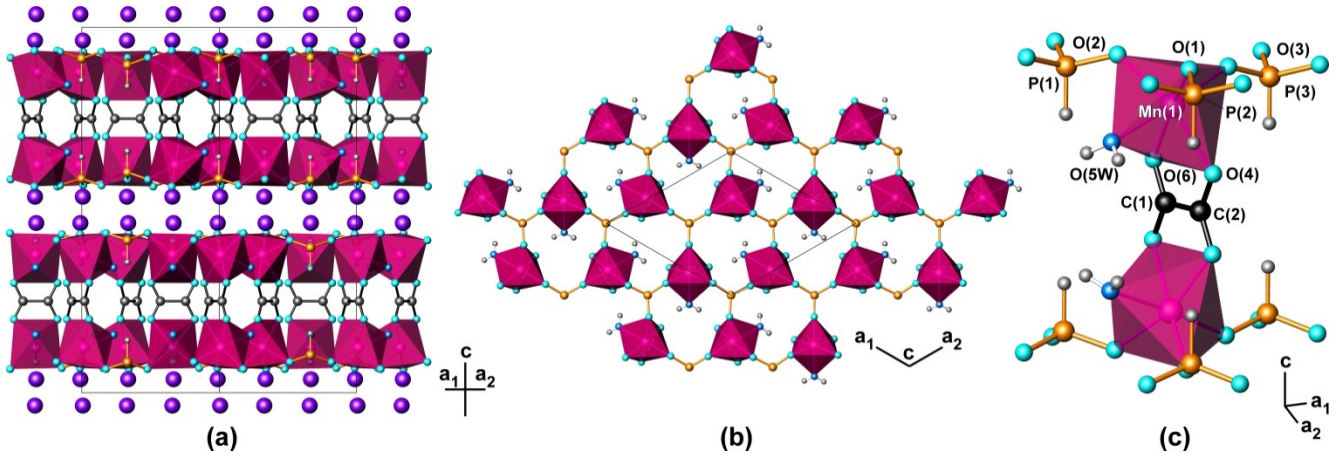

Fig. 1 a) Polyhedral plot of the two-dimensional structure of **KMnCP**. Color code: $MnO_5(H_2O)$ octahedra, pink; $[HPO_3]^{2-}$ pseudo-pyramids, orange; oxygen, blue; carbon, black; potassium, purple, hydrogen, grey. b) A view of the 2D anionic double layer along the [001] direction. c) Detail of the coordination environment of Mn(1) and the bridging by the oxalate. (For interpretation of the reference to color in this figure legend, the reader is referred to the web version of this article).

From a topological point of view, the double-layered honeycomb sheets of **KMnCP** can be represented as a binodal (3,4)-connecting net with a point symbol of $\{6^3\}\{6^6\}$, in which Mn(1) is considered as a 4-connecting node and the three crystallographically independent phosphorous atoms are 3-connecting nodes. After this simplification a known topology type 3,4L147 is obtained (Fig. 2). Such underlying net is not very frequent. In fact, it has only been reported in three compounds, such as in a Cd(II) coordination polymer [32] as an interpenetrated topology and in two lanthanide MOFs[33] as not interpenetrated frameworks (Fig. S6). As can be seen in the comparative view of Fig. 2, **KMnCP** displays hexagonal graphite-like honeycomb double-layers stacked in an ABAB sequence where the double-layers are related by a binary screw axis, in contrast with the lantanide MOFs that show a double-layered pattern made of irregular hexagons.

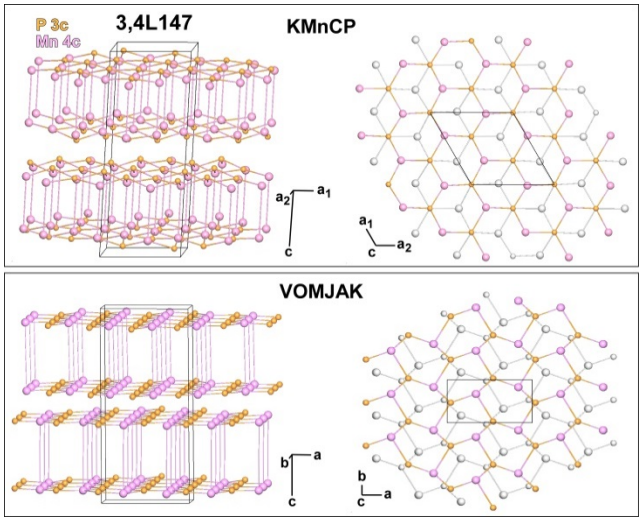

Fig. 2 Topological views of the double-layered honeycomb sheets of **KMnCP**. Color code: Mn(1) nodes, pink; phosphorous nodes, orange. Layers with gray color in top view represent the second double-layered sheet inside the colored one. Comparative view of the not interpenetrated 3,4L147 topology previously reported, VOMJAK.

This journal is © The Royal Society of Chemistry 20xx

Please do not adjust margins

Crystal growth

The predicted equilibrium morphology of **KCMnP** shown in Fig. 3, is a hexagonal prism with (001) basal face and {hk0} prismatic faces with truncated edges. Experimentally, two different crystal habits can be distinguished. The major fraction of crystals displays hexagonal plate habits. These plate crystals are accompanied by some hexagonal prism morphologies, whose (001) faces exhibit clearly smaller areas which is in good agreement with a preferential growth of the {hk0} faces along the c-axis direction. According to the Gibbs-Curie-Wulff theorem[34], the surface free energies play essential roles in the crystal growth processes. Since the main habit are hexagonal platelets, the {001} basal planes have the lowest surface energy and the slowest growth rate, while the six lateral planes grow faster with an equivalent rate.

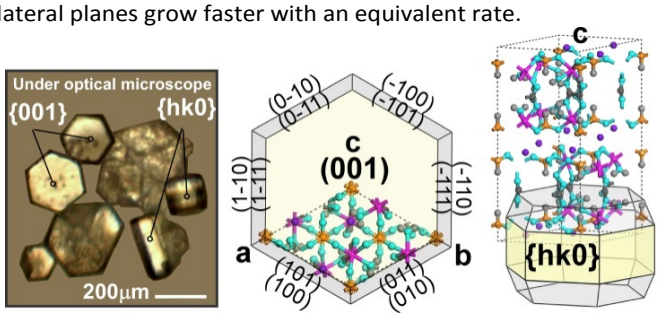

Fig. 3 Crystal habits under optical microscopy and predicted growth morphology of **KMnCP** crystal.

Although length to width proportion of the crystals generally increases with crystallization temperature, the final size and shape of the crystals formed at a given temperature depend on many parameters that affect the values of the apparent activation energies, and thus the growth rates of different crystal faces. As a symmetry-based method, BFDH produce valuable information to limit the number of possible growing faces to be studied by the more expensive and demanding energy-based approaches.[35] Nevertheless, some computational studies on quinoline derivatives establish that symmetry constraints of the more symmetric systems make BFDH predictions more realistic than in lower symmetry ones[36]. Since **KMnCP** crystallizes in a high symmetry space group ($P6_3/m$), we assume that our morphology prediction based on BFDH laws is a realistic approximation in a good agreement with the as-grown crystals observed in Fig. 3.

J. Meng et al.[37] studied the synergistic effect between vanadium oxide layer surface configurations and the K ions in terms of electrochemical stability. While the layer surface of KV_3O_8 is composed of single- and tri-connected oxygen atoms, all of them on the layer surface of $K_{0.25}V_2O_5$ are single-connected, which can bond and provide strong interaction with K ions. So, more strongly bonded K ions in the interlayers act as pillars to maintain the structural integrity. In our case, the oxygen atoms that establish bonds with the potassium ions on the double-layered sheets surfaces are di-connected (O(1), O(2) and O(3)) to the manganese and phosphorous atoms and single-connected in the case of the coordinated water molecule. In terms of crystal growth dynamics potassium layers should be the most probable endings for basal faces, in such a way that the crystal growth is preferential in *a* and *b* axis (Fig. S7) as can be seen in the preferential crystallization as hexagonal plates.

Structural classification

In order to better understand the metal-phosphite-oxalate structural chemistry, a crystallo-chemical revision of the crystal architectures constructed from metal phosphites containing HPO_3 groups and oxalate bridges have been carried out (22 archetypes found at August 10th, 2017 in the Cambridge Structural Database (CSD)[38]). The structures have been analyzed based on their metal phosphite framework, as well as by the role of the oxalate anion. Several common characteristics have been found:

i) All the metal-phosphite oxalate frameworks have negative charge needed to be compensated by a cationic inorganic or organic template.

ii) The metal-phosphite substructures can be described based on seven different Structural Building Units (SBUs) showed in Fig. 4. Each SBU has been denoted taking into account the number of metal polyhedra and phosphite groups.

iii) The most common SBU observed in more than the half of the crystal structures is the M_2P_2-cycle, the basic building block for several observed chains, layers and even some 3D inorganic frameworks.

iv) Depending on the connectivity between a single or multiple SBUs, 1D to 3D inorganic scaffolds have been found.

v) The oxalate group can act in a mono-bidentate mode, chelating the metal centers, or in a bis-bidentate fashion acting as a bridge between the metal centers of the inorganic framework.

vi) As a general rule, the connectivity of the inorganic substructures through the oxalate ligand gives rise to an increase of the crystal structure dimensionality. This is reflected in the high number of 2D and 3D structures in comparison with the 1D or 0D ones.

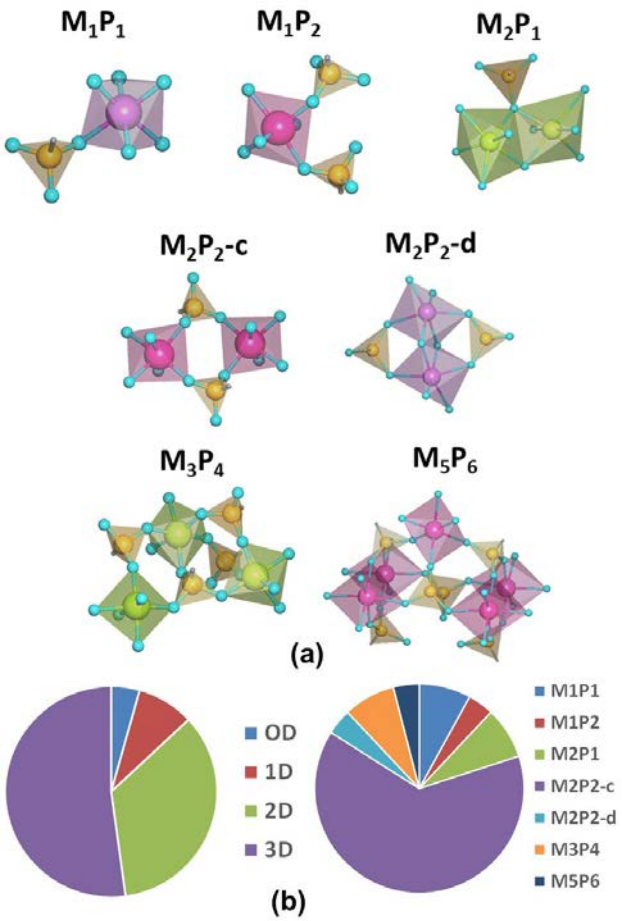

Fig. 4 (a) Polyhedral representation of the different SBUs found in metal oxalatophosphites. M and P represent the number of metal polyhedra and HPO_3 units respectively. (b) Distribution of the dimensionality and the various SBUs found in the classified compounds.

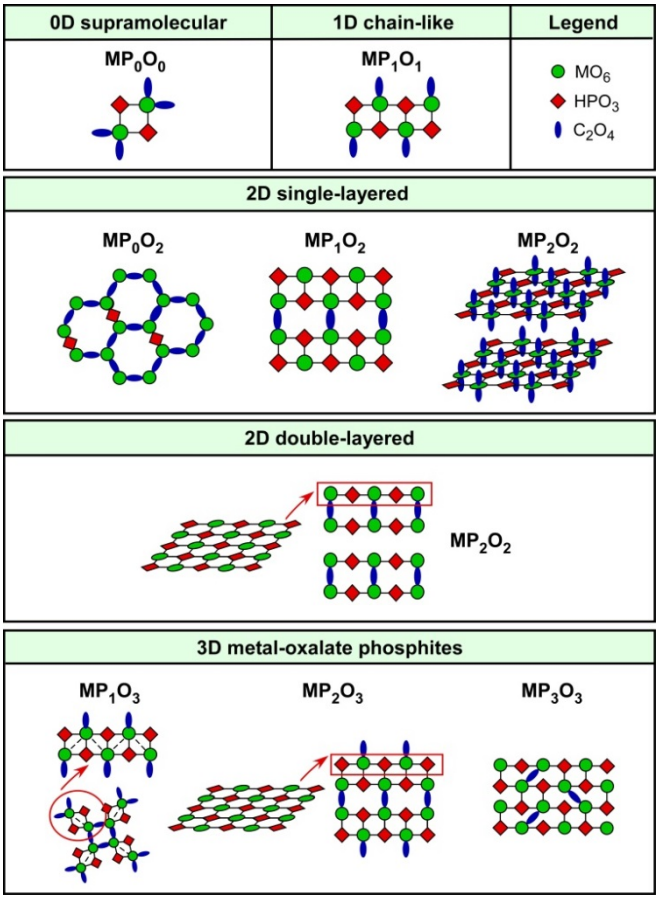

Fig. 5 Schematic representation of the different structural archetypes observed in metal oxalatophosphites with anionic frameworks.

Table 2 summarizes the formula, SBU unit, oxalate role and a brief description of the crystal structure. In the last column of the table the compounds have been classified according to the dimensionality of the inorganic metal phosphite skeleton and the role of the oxalate in the structures. (follow Fig. 5 for structural classification and Fig. S8 for structural visualization of the analyzed compounds). A two letter based code has been assigned to each structure, MP_xO_y. MP stands for metal-phosphite, and O for oxalate. *x* defines the dimensionality of the inorganic metal phosphite net and *y* the dimensionality of the complete inorganic-organic net considering the connectivity of the metal centers through the oxalate bridges. Based on the proposed MP_xO_y code, nine crystal architectures depicted in Fig. 5 have been identified.

There is only an example of MP_0O_0 discrete clusters, which can be also described as M_2P_2 cycles with oxalate groups chelating the metal centers. The extension along one direction of the M_2P_2 cycles found in the abovementioned zero-dimensional metal oxalatophosphite gives rise to ladder-like MP_1O_1 chained structures.

The MP_0O_2 archetype presents a honeycomb-like layer usually found in transition-metal oxalates. In the special case of the unique compound found within this group, the metal-oxalate net is partially interrupted by phosphite linkages. The interlinking of the ladder-like M-O-P chains through bis-bidentate oxalate ligands in-plane fashion form 2D anionic layers found in MP_1O_2 compounds.

When the connectivity of the inorganic chains is given by oxalate bidentate bridges in- and out-of-plane fashions a three dimensional crystal structure can be formed, such as in the MP_1O_3 crystal architectures.

Metal phosphite layers are commonly observed in inorganic-organic phosphites, but the role of the oxalate group determines the effective connectivity of the 2D sheets in 3D arrangements. For MP_2O_2 the oxalate acts commonly as mono-bidentate units projected on both sides of the sheets, preventing the pillaring of the inorganic layers through covalent bridges. A special case of MP_2O_2 architecture is the title compound, in which the oxalate units act as bis-bidentate ligand, but their connectivity is limited to two adjacent layers, giving rise to the doubled inorganic-organic substructure described above.

This journal is © The Royal Society of Chemistry 20xx

CrystEngComm

ARTICLE

Table 2 Metal oxalatophosphites with anionic frameworks. Metal-phosphite inorganic SBUs together with the role of the oxalate to get the dimensionality of the final archetype

Compound	Metal-HPO_3 SBU	Oxalate	Class.	Ref.
0-dimensional				
$(C_4N_2H_{12})_3[In_2(HPO_3)_2(C_2O_4)_4]\cdot 4H_2O$	M_2P_2 cycles	Mono-bidentate terminal unit	MP_0O_0	[5c]
1-dimensional				
$(C_6N_2H_{14})_2[Ga_2(OH)_2(C_2O_4)_2(HPO_3)_2]\cdot 2H_2O$ $(C_6N_2H_{14})_2[Fe^{III}{}_2F_2(HPO_3)_2(C_2O_4)_2]\cdot 2H_2O$	M_2P_2 ladder-like chains formed by corner linked M_2P_2 cycles	Mono-bidentate terminal unit	MP_1O_1	[9c] [8a]
2-dimensional (single layers)				
$(C_6N_4H_{21})_2[Fe^{II}{}_4(HPO_3)_2(C_2O_4)_5]\cdot 5H_2O$	M_2P_2 cycles	Some oxalate units are replaced by phosphite linkers in a 2D metal-oxalate net	MP_0O_2	[8a]
$(C_6N_2H_{18})_{0.5}[Ga(OH)(C_2O_4)_{0.5}(HPO_3)]$ $A_2[(VO)_2(HPO_3)_2(C_2O_4)]\cdot nH_2O$ (A=Li, Na, K, NH_4)	M_2P_2 ladder-like chains formed by corner linked M_2P_2 cycles	Bridges metal centers of adjacent inorganic chains	MP_1O_2	[9c] [12a,b]
$(C_6N_2H_{16})[Ga_2(HPO_3)_2(H_2PO_3)_2(C_2O_4)]$ $[H_2apm][Ga_2(HPO_3)_2(H_2PO_3)_2(C_2O_4)]$	M_2P_4 chains formed by M_2P_2 cycles linked through phosphite groups			[9a,b]
$(C_4N_2H_{12})_2[In_2(HPO_3)_3(C_2O_4)_2]\cdot 3H_2O$	M_1P_2 chains linked through M_2P_2 cycles	Chelates metal centers in both sides of the layers	MP_2O_2	[5c]
2-dimensional (double layers)				
$K_2[Mn^{II}{}_2(H_2O)_2C_2O_4(HPO_3)_2]$	M_1P_1 hexagonal layers	Bridges metal centers of two adjacent single layers	MP_2O_2	This Work
$(C_4N_2H_{12})_3[In_4(HPO_3)_6(C_2O_4)_3]$	M_2P_2 chains generated from corner linked M_2P_2 cycles interconnected by phosphite units	Dual role bridging adjacent layers in a bilayer arrangement and acting as terminal units	MP_2O_2	[5c]
3-dimensional				
$(C_4N_2H_{12})[M^{II}{}_4(HPO_3)_2(C_2O_4)_3]$ (M= Fe, Co) $(C_5N_2H_{14})[Fe^{II}{}_4(HPO_3)_2(C_2O_4)_3]$	M_2P_1 chains of edge shared metal dimmers capped by a phosphite group	Each chain connects four adjacent ones through oxalate bridges	MP_1O_3	[8a,b] [6a]
$(CN_3H_6)_2\cdot Mn^{II}{}_{2.5}(HPO_3)(C_2O_4)_{2.5}(H_2O)\cdot H_2O$	M_5P_2 chains formed by M_2P_2 cycles linked through metal octahedra. Chains are decorated by two metal octahedra	Each chain connects four adjacent ones through oxalate bridges	MP_1O_3	[7a]
$[C_4N_2H_{12}][In_2(HPO_3)_3(C_2O_4)]$	M_2P_2 chains generated from corner linked M_2P_2 cycles interconnected by phosphite units	Connects metal centers of adjacent layers	MP_2O_3	[5b]
$H[In_5(HPO_3)_6(H_2PO_3)_2(C_2O_4)_2]\cdot(C_4N_2H_{11})_2\cdot H_2O$	M_5P_6 clusters connected in a 1D array. Phosphites link adjacent chains		MP_2O_3	[5a]
$(C_4N_2H_{12})[Mn^{II}{}_2(HPO_3)_2(C_2O_4)]$	Corner linked 4-connected M_2P_2 tetrammers		MP_2O_3	[7d]
$(C_2N_2H_{10})[M^{II}{}_2(OH_2)_2(HPO_3)_2(C_2O_4)]$ (M= Mn, Fe)	Corner linked 4-connected M_2P_2 cycles		MP_2O_3	[7c] [8a]
$(H_2dab)[Mn_2(HPO_3)_2(C_2O_4)(H_2O)_2]$	M_1P_1 hexagonal layers		MP_2O_3	[7b]
$(C_6N_2H_{16})_{0.5}[Ga_2(HPO_3)_2(H_2PO_3)(C_2O_4)]$	Dimmers of corner-linked M_2P_2 cycles	Acts as a intralayer connector of metal centers	MP_3O_3	[9b]
$(C_6H_{14}N_2)[In_2(HPO_3)_3(C_2O_4)]$	Corner linked M_2P_2 cycles		MP_3O_3	[5d]
$(C_8N_4H_{26})[Fe^{III}{}_6(HPO_3)_8(C_2O_4)_3]\cdot 4H_2O$	Corner linked six connected M_3P_4 clusters	Dual role acting as in- and out-of-plane bridging units	MP_3O_3	[8a]
$(C_4N_2H_{14})[In_4(H_2O)(HPO_3)_5(C_2O_4)_2]\cdot 2H_2O$	Corner linked M_3P_4 clusters and M_2P_2 cycles		MP_3O_3	[5c]

When the connectivity of the bis-bidentate oxalate ligands is extended through all the inorganic layers a MP_2O_3 crystal architecture is generated. The nature of the metal-phosphite inorganic layers found in MP_2O_3 and MP_3O_3 type structures is quite diverse, and can be formed by corner shared M_2P_2 cycles, M_2P_2 dimmers, M_3P_4 clusters or even corner linked M_5P_6 cages. When the inorganic framework is three dimensional, MP_3O_3, it is not possible a dimensionality increase through the oxalate groups, but they act as organic pillars connecting metal centers within the inorganic substructure.

Through this literature little review and subsequent classification we have shown the different roles that the oxalate anion adopts in the formation of different structural

Please do not adjust margins

types and the possible relationships between them and their resulting dimensionality in compounds based on metal oxalato-phosphites with anionic structures. So, in a general view, terminal oxalates are found mainly in zero- and one-dimensional structures. The connection of chains trough bis-bidentate oxalate units in an in-plane fashion gives rise to two-dimensional layers. The stacking of the layers by oxalate moieties out-of-plane can complete the three-dimensional connectivity or generate a special structural feature as the double-layered two-dimensional structure found in the studied compound, **KMnCP**.

Thermal study

The thermal decomposition can be described as a three-step process. The initial weight loss (~8.2%) observed between 175 ºC and 300 ºC corresponds to the departure of two coordinated water molecules (7.63% calculated) per unit formula. From this point to 350 ºC an abrupt weight loss (~7.9%) associated with the thermal breakdown of some oxalate moieties is observed. Such process is marked by a sharp exothermic peak at 335 °C on the DSC curve. The third step of weight loss (~4.2%), in the 350-500ºC temperature range, follows ascribed to the oxalate units release. Finally, up to 800ºC only 0.5% of mass is lost (see Fig. S.9(a)). The final decomposed product of **KMnCP** identified by powder XRD was $KMnPO_4$[39] (S.G. P-1 (2), a= 5.4813(5) Å, b= 8.6274(10) Å, c= 8.8865(13) Å, α= 87.728(10)º, β= 89.101(10)º, γ= 88.009(10)º) with some other less intense peaks of an unidentified phase (Fig. S.9(b)). The calculated weight loss due to decomposition of water molecules and oxalate unit is 26.27%, but the observed weight loss was only 20.74%. This discrepancy can be explained by considering the oxidation of P(III) to P(V) during the decomposition. In parallel, the studied compound was calcined at 800ºC in argon atmosphere obtaining $KMnPO_4$ as pure phase (Fig. S.9(b)). So it is possible that the unidentified extra peaks observed in the diffractogram of the TGA calcination product are due also to an oxidation process supporting the difference between the observed and the calculated weight loss.

The thermodiffractometry in air of **KMnCP** shows that the diffraction peaks of the phase remain unchanged until 225 ºC, then decreasing in intensity until disappearing at 285 ºC (Fig. S10). So the crystalline structure of the compound collapses due to the coordinated water molecule decomposition, as observed in the TGA study.

Infrared, Raman and UV-Vis spectroscopy

A vibrational spectroscopic study was carried out to advance in a better knowledge in the structure of **KMnCP** (Fig. S11 and Table S2). IR spectrum confirms the existence of the $(HPO_3)^{2-}$ groups by the presence of three sharp bands situated at 2402 cm^{-1}, 2344 cm^{-1} and 1018 cm^{-1} (IR and Raman) corresponding to the stretching vibrational mode and deformation of the P-H bond (Fig. S.11(b)). The P-O bonds vibrations of such phosphite moieties are found at frequencies below 1100 cm^{-1} (see Fig. S.11(a)). The comparison of the IR and Raman vibrational spectra (Fig. S11) shows that the differences in the intensities of the bands and the shifts in their positions are considerably more pronounced for the vibrational modes of the organic ligand, oxalate, than for the inorganic part represented by the phosphite units. For instance, the ν_{as}(C-O) vibrations of the oxalate group are found at the same energies, 1714 (Raman: 1713 cm^{-1}) and 1635 cm^{-1}, in IR and Raman spectra, but the intensity in 1714 cm^{-1} is significantly stronger in the IR spectrum in comparison with Raman signal, which is very weak. Additionally, ν_s(C-O) vibrations (IR: 1360 cm^{-1}, 1318 cm^{-1}, Raman: 1480 cm^{-1}, 1440 cm^{-1}) are shifted around 120 cm^{-1} to higher energies in Raman counterpart. And the same phenomenon is observed for the δ(OCO) vibrational mode, in this case with a lower shift of around 50 cm^{-1} (see Fig. S.11(a) and Table S2). Finally, The ν(O-H) stretching vibration of the coordinated water molecule appears as a very strong absorption centered at 3275 cm^{-1} (IR) (Fig. S.11(b)), which is consistent with the relatively strong character of the hydrogen bond inferred from the structural analysis, where the O-H···O distances are around 2.67 Å. And furthermore, the weak bands situated around 748 cm^{-1} and 723 cm^{-1} (IR) could be tentatively associated to the librational modes of the coordinated water in accordance with a previous study on a dihydrated iron(II) oxalate where the 755/714 cm^{-1} doublet disappears after deuteration.[40]

The diffuse reflectance spectrum exhibits three weak spin-forbidden *d-d* bands, at approximately 403, 437 and 530 nm similar to those of other octahedrally coordinated Mn^{2+} complexes which correspond to transitions from the $^6A_1(^6S)$ ground state to $^4E(^4G)$, $^4T_2(^4G)$ and $^4T_1(^4G)$ terms (Fig. S12(a)). The *Dq* and Racah parameters for an octahedral d^5 high-spin system[41] cannot be calculated because the frequencies of the transitions to $^4T_2(^4D)$ or $^4E(^4D)$, needed for the calculation and usually found at higher energies, are strongly forbidden and do not appear in the spectrum.

Absorption (K/S) data were calculated from the following Kubelka-Munk function:[42]

$$F(R) = (1 - R)^2/2R = K/S \quad (1)$$

with *R* representing the reflectance, *K* the absorption, and *S* the scattering. In a *K/S* vs *E* (eV) plot (Fig. S12(b)), extrapolating the linear part of the rising curve to zero provides the onset of absorption. The value of energy band gap calculated is 3.08 eV.

Electronic structure

The electronic structure of **KMnCP** was studied systematically through the DFT calculation of the band structure and total density of states (TDOS) (Fig. S13). The distance from the top of the valence band (VB) and bottom of the conduction band (CB) determines the energy necessary for an electron to move from VB to CB which is known as band gap. The band structure of the compound reveals the direct band gap with the top of the VB and bottom of the CB at Γ point. The CB electrons are contributing more at the Fermi level than the VB electrons, which indicates that the crystal belongs to p-type semiconductors with the narrow band gap of 0.027 Ha (0.73eV). Further insight into the electronic structure we examined the partial density of states (PDOS) for all the elements: Mn, P, K, C, H, and O (Fig. S14). In PDOS, the

 This journal is © The Royal Society of Chemistry 20xx

Please do not adjust margins

Please do not adjust margins

significant contributions of top of the VB are from Mn-3d and O-2p states which confirm the hybridization between p-d states of Mn-O atoms. Similarly the VB composed of P-2p and O-3p is in the range of -0.2 to -0.4 Ha and -0.8 to -0.7 Ha, K-2p and O-2p mixing is from -0.49 to -0.54 Ha, C-2p with O-2p from 0.4 to -0.5 Ha and H-1s and O-2p hybridization is found from 0.7 to -0.8 Ha. The spins in the bottom of the CB is mostly composed of O-2p states with a small contribution of C-2p states. Hence the Mn-3d states act as electron acceptors which show more contribution at VB region near at fermi level and the O-2p as electron donors. Hence, the optical activity of the crystal is originated by the electronic transition from Mn-3d to O-2p states.

Magnetic behaviour

The temperature dependence of the molar magnetic susceptibility (χ_m) measurement was performed on powdered sample of **KMnCP** from 250 to 5 K, in the Zero Field Cooling (ZFC) mode at 1 kOe. The thermal evolution of χ_m follows the classical Curie−Weiss law above 13 K, with Weiss temperature θ_p =−20.6 K and Curie constant C_m = 4.80 emu·K/Mn-mol·Oe. The effective paramagnetic moment (μ_{eff}) value calculated for the paramagnetic region, $\mu_{eff} = 2.828(C_m)^{1/2}$, gives the value of 6.19 μ_B/Mn^{2+} ion, very close to the theoretical one (μ_{eff} = 5.91 μ_B) obtained from $\mu_{eff} = g[S(S = 1)]^{1/2}$, considering high-spin S = 5/2 Mn^{2+} cations with no orbital contribution.

χ_m increases from 250 K as temperature decreases describing a smooth inflection point at low temperature. The negative θ_p value, together with the reduction of the effective magnetic moment (χ_mT) observed when the temperature is decreasing (lower inset of Fig. S.15) suggests global antiferromagnetic interactions. ZFC and subsequently FC measurements were also carried out under 100 Oe at low temperatures (upper inset of Fig. S.15). The curves do not show a clear maximum but an inflection point at around 10K, defining the Neel temperature. Moreover, no irreversibility is observed, discarding the existence of any ferromagnetic interaction.

Taking into account the crystal structure, the most probable magnetic exchange pathways due to the Mn···Mn distances and number of atoms involved in the paths are:

i) ***J1*** **(Mn-O-P-O-Mn)**: within the manganese-phosphite single inorganic layers, the Mn(II) cations are connected through phosphite pseudo-tetrahedra defining a hexagonal honeycomb Mn(II) layer. Mn···Mn intralayer distances takes three different values, 5.484, 5.513 and 5.878 Å. In an ideal honeycomb layer, the Mn(II) atoms would be spaced by the same distance, but the inorganic layers of the studied compound show a distortion in which the Mn(II) cations are grouped in triangular clusters with the abovementioned Mn···Mn spacing (Fig. S16).

ii) ***J2*** **(Mn-O-C-O-Mn)**: manganese cations of each individual inorganic layer are connected through the oxalate organic ligand to the adjacent one, defining Mn-Ox-Mn interlayer dimmers with Mn···Mn bond distances of 5.725 Å.

J1 and J2 involve very similar Mn···Mn distances, and the same number of atoms in the magnetic pathway, so most probably both of them are effective within the same range of temperatures. Magnetic exchange through potassium cations (***J3***) is expected to be less effective at high temperatures, with Mn···Mn distances of 6.373 Å, but short enough to be involved in a magnetic ordered structure at low temperatures.

So, bearing the crystallographic information in mind we have tried to fit the magnetic data to a honeycomb hexagonal Heisenberg layer model, and to a manganese dimmers model taking into account an intermolecular J´ exchange. These models are near to the experimental data, but far from describing a reasonable model from the obtained J values. For both attempts, g values near 2 are obtained, in good agreement with the isotropic electronic nature of high-spin S = 5/2 Mn^{2+} cations. The positive J exchange value result from the honeycomb layer Heisenberg model fitting (Fig. S17) is opposite to the antiferromagnetic behavior observed in the decreasing χ_mT curve (lower inset of Fig S.14)).

When an intra- and inter- dimeric magnetic exchange is considered, J = -0.97(1) K and J´ = -4.28(10) K values are obtained. In an ideal intra- and inter-dimmer exchange, J would be at least one order of magnitude greater than J´, but in the specific case of **KMnCP,** the J1 and J2 exchange are too similar to be considered as intra- and inter-dimmer contributions. Considering only the intra-dimmer magnetic exchange in the fitting a value of J=-1.63(2) K is obtained, and the fitting is not too far from the experimental data. It is clear that the J values obtained from these dimmer based models are not accurate, but the negative values obtained for the fittings are in good agreement with the antiferromagnetic behavior derived from the Weiss temperature.

There is a need to seek a more complex theoretical model or neutron diffraction experiments to obtain a correct magnetic model. In fact the Neel ordering suggested by the magnetic susceptibility is not trivial. Examples of the great variety and complexity of magnetic interactions and possible antiferromagnetic orderings in this type of hexagonal systems are the metal-oxalate layered coordination compounds,[43] the inorganic metal halides[44] or some transition metal oxides[45] showing centered hexagonal honeycomb metal layers. In fact, the complexity of the magnetic exchange/ordering in the title compound could be even greater, giving the fact that the single honeycomb layers are connected also by the oxalate groups, and that the magnetic exchange through the potassium cations could become effective also at low temperatures.

Conclusions

In summary, we have reported the synthesis and characterization of a novel 2D manganese(II) phosphite with anionic framework containing oxalate bridges. BFDH analysis turned out to be a realistic approximation to compare the predicted morphology with the hexagonal plates and prisms morphologies experimentally observed.

The role of the oxalate generally determines the final dimensionality of the archetype. In that sense, the special bilayer arrangement observed in the structural study of **KMnCP** is consequence of the connection of two single sheets

Please do not adjust margins

Please do not adjust margins

through bis-bidentate oxalate units in an out-of-plane fashion. The three-dimensional connectivity observed in other compounds, is disrupted in this case by the interlayer spaces occupied by the potassium counter ions. The manganese octahedra join in-plane with 3-connecting HPO_3 groups and out-of-plane with other metal octahedron through the oxalate unit giving rise to the double-layered honeycomb sheets with not very frequent 3,4L147 topology, previously observed in a coordination polymer and two metal-organic frameworks.

Such special features have motivated us to revise the structural chemistry of the metal oxalatophoshites with anionic frameworks. Several Secondary Building Units (SBUs) formed by metal-phosphite substructures and different roles of de oxalate bridges have been described promoting a new structural classification for the mentioned compounds. M_2P_2-cycle is the most common basic building block observed in more than the half of the crystal structures. The connectivity of the inorganic substructures through the oxalate ligand generally gives rise to an increase of the crystal structure dimensionality, which is obvious from the prevalence of 2D and 3D structures in comparison with mono-dimensional or supramolecular ones.

With a broader view, the crystallo-chemical analysis here developed could be extrapolated for other tetrahedral (phosphate, arsenate, sulfate or vanadate) or pseudotetrahedral (selenite, tellurite or sulfite) metal hybrid phases containing short organic linkers.

Finally, **KMnCP** displays major antiferromagnetic interactions. Neutron diffraction experiments to obtain a correct magnetic model is needed since magnetic data fitting to honeycomb hexagonal Heisenberg layers model or to a manganese dimmers model are near to the experimental data but far from a real situation.

Conflicts of interest

There are no conflicts to declare.

Acknowledgements

This work has been financially supported by the “Ministerio de Economía y Competitividad” (MAT2016-76739-R (AEI/FEDER, EU)), the “Gobierno Vasco” (Basque University Research System Group, IT-630-13 and Economic Development and Competitiveness, ACTIMAT (KK-2015/00094), ELKARTEK program) which we gratefully acknowledge. Joseba Orive wishes to thank CONICYT for the FONDECYT postdoctoral project (N^{er} 3150455). The authors thank the technicians of SGIker (UPV/EHU) and Franck Quero from Universidad de Chile for Raman measurements.

Notes and references

‡ CCDC 1573595.

1 1(a) Y. Cui, B. Li, H. He, W. Zhou, B. Chen and G. Qian, *Acc. Chem. Res.*, 2016, **49(3)**, 483; (b) L. Wang, Y. Han, X. Feng, J. Zhou, P. Qi and B. Wang., *Coord. Chem. Rev.*, 2016, **307(Part 2)**, 361; (c) V. Stavila, A. A. Talin and M. D. Allendorf, *Chem. Soc. Rev.*, 2014, **43(16)**, 5994; (d) J. Liu, L. Chen, H. Cui, J. Zhang, L. Zhang and C-Y. Su, *Chem. Soc. Rev.*, 2014, **43(16)**, 6011; (e) H. Furukawa, K. E. Cordova, M. O'Keeffe and O. M. Yaghi, *Science*, 2013, **341(6149)**, 974; (f) Z. Zhang, Y. Zhao, Q. Gong, Z. Li and J. Li, *Chem. Comm.*, 2013, **49(7)**, 653.

2 2(a) D. Maspoch, D. Ruiz-Molina and J. Veciana, *Chem. Soc. Rev.*, 2007, **36**, 770; (b) S. Natarajan and S. Mandal, *Angew. Chem. Int. Ed.*, 2008, **47**, 4798; (c) C. N. R. Rao, S. Natarajan and R. Vaidhyanathan, *Angew. Chem. Int. Ed.*, 2004, **43**, 1466.

3 3(a) Y-C. Yang and S-L. Wang, *J. Am. Chem. Soc.*, 2008, **130(4)**, 1146; (b) Y-C. Jiang, S-L. Wang, S-F. Lee and K-H. Lii, *Inorg. Chem*., 2003, **42(20)**, 6154; (c) J. Do, R. P. Bontchev and A. J. Jacobson, *Chem. Mater.,* 2001, **13(8)**, 2601; (d) Y-C. Jiang, S-L. Wang, K-H. Lii, N. Nguyen and A. Ducouret, *Chem. Mater.*, 2003, **15(8)**, 1633; (e) N. Rajic, N. Z. Logar, G. Mali and V. Kaucic, *Chem. Mater.,* 2003, **15(8)**, 1734.

4 4 T. Rojo, J. L. Mesa, J. Lago, B. Bazán, J. L. Pizarro and M. I. Arriortua, *J. Mater. Chem.*, 2009, **19**, 3793.

5 5(a) M. Zuo, M. Zhou, D. Hu, F. Gao, S. Dong and L. Huang, *J. Solid State Chem.*, 2016, **237**, 219; (b) H. Li, L. Zhang, Q. Huo and Y. Liu, *J. Solid State Chem.*, 2013, **197**, 75; (c) P. Ramaswamy, N. N. Hegde, R. Prabhu, V. M. Vidya, A. Datta and S. Natarajan, *Inorg. Chem.*, 2009, **48(24)**, 11697; (d) H. Li, L. Zhang, L. Liu, T. Jiang, Y. Yu, G. Li, Q. Huo and Y. Liu, *Inorg. Chem. Comm.*, 2009, **12(10)**, 1020.

6 6(a) S. Mandal and S. Natarajan. *J. Solid State Chem.* 2005, **178(7)**, 2376.

7 7(a) L. Liu, D. Luo, D. Li and Z. Lin, *Dalton Trans.*, 2014, **43(21)**, 7695; (b) Z. Lin, H. P. Nayek and S. Dehnen, *Micropor. Mesopor. Mat.*, 2009, **126(1-2)**, 95; (c) P. Ramaswamy, S. Mandal and S. Natarajan, *J. Solid State Chem.*, 2009, **182(9)**, 2491; (d) S. Mandal, M. A. Green, S. K. Pati and S. Natarajan, *J. Mater. Chem.,* 2007, **17(10)**, 980.

8 8(a) S. Mandal and S. Natarajan, *Chem-Eur J.*, 2007, **13(3)**, 968; (b) S. Mandal, S. K. Pati, M. A. Green and S. Natarajan, *Chem. Mater.*, 2005, **17(11)**, 2912.

9 9(a) Z-Z. Xue, J. Pan, J-H. Li, Z-H. Wang and G-M. Wang, *J. Mol. Struct.*, 2017, **1138**, 1; (b) C. Li, L. Huang, M. Zhou, J. Xia, H. Ma, S. Zang and L. Wang, *J. Solid State Chem.,* 2013, **208**, 86; (c) G-P. Zhou, Y-L. Yang, R-Q. Fan, X-R. Liu, Q. Wang and F-P. Wang, *Solid State Sciences*, 2010, **12(5)**, 873.

10 10 C-M. Wang, Y-Y. Wu, Y-W. Chang and K-H. Lii, *Chem. Mater.*, 2008, **20(9)**, 2857.

11 11(a) X. Yang, J. Li, Y. Hou, S. Shi and Y. Shan, *Inorg. Chimica Acta*, 2008, **361(5)**, 1510; (b) C-Y. Sheu, S-F- Lee and K-H. Lii, *Inorg. Chem.*, 2006, **45(5)**, 1891; (c) J. F. Colin, T. Bataille, S. E. Ashbrook, N. Audebrand, L. Le Polles, J. Y. Pivan and E. Le Fur, *Inorg. Chem.*, 2006, **45(15)**, 6034; (d) L-C. Hung, H-M. Kao and K-H. Lii, *Chem. Mater.*, 2000, **12(8)**, 2411.

12 12(a) C. Kouvatas, V. Alonzo, T. Bataille, L. Le Pollès, C. Roiland, G. Louarn and E. Le Fur, *J. Solid State Chem.*, 2017, **253**, 73; (b) A. Shahul Hameed, M. V. Reddy, N. Sarkar, B. V. R. Chowdari and J. J. Vittal, *RSC Adv.*, 2015, **5**, 60630; (c) S. Auguste, V. Alonzo, T. Bataille, L. Le Polles, W. Canon-Mancisidor, D. Venegas-Yazigi and E. Le Fur, *J. Solid State Chem.*, 2014, **211**, 212.

13 13 M. Nagarathinam, K. Saravanan, E. J. H. Phua, M. V. Reddy, B. V. R. Chowdari and J. J. Vittal, *Angew. Chem., Int. Ed.*, 2012, **51**, 5866.

 This journal is © The Royal Society of Chemistry 20xx

Please do not adjust margins

Please do not adjust margins

14 14 A. S. Hameed, M. Nagarathinam, M. Schreyer, M. V. Reddy, B. V. R. Chowdaric and J. J. Vittal, *J. Mater. Chem. A*, 2013, **1**, 5721.
15 15 J. **Orive**, R. Fernández de Luis, J. Rodríguez Fernández, L. Lezama, M. I. Arriortua, *Dalton Trans.*, 2016, **45**, 12188.
16 16 P. Román and J. M. Gutiérrez-Zorrilla, *Chem. Educ.*, 1985, **62**, 167.
17 17 W. Yingua, *J. Appl. Crystallogr.*, 1987, **20**, 258.
18 18 A. C. T. North, D. C. Philips and F. S. Mathews, *Acta Crystallogr.*, 1968, **A24**, 351.
19 19 *CrysAlisPro CCD* and *RED*, version 171.35.19; Oxford Diffraction, Ltd.: Oxford, U.K., 2011.
20 20 G. M. Sheldrick, *SHELXS 97: Program for the Solution of Crystal Structures*, University of Göttingen, Germany, 1977.
21 21 G. M. Sheldrick, *SHELXL 97: Program for the Refinement of Crystal Structures*, University of Göttingen, Germany, 1977.
22 22 L. J. Farrugia, *J. Appl. Crystallogr.*, 1999, **32**, 837.
23 23 A. L. Spek, *PLATON94: Program for the Automated Analysis of Molecular Geometry*, University of Utrecth, The Netherlands, 1994.
24 24 E. Dowty, *ATOMS: A Computer Program for Displaying Atomic Structures*, Shape Software, 512 Hidden Valley Road, Kingsport, TN, 1993.
25 25 J. Rodriguez-Carvajal, *Phys. B*, 1993, **192**, 55.
26 26 I. D. Brown and D. Altermatt, *Acta Crystallogr.*, 1985, **B41(4)**, 244.
27 27 (a)S. Álvarez, D. Avnir, M. Llunel and M. Pinsky, *New. J. Chem.*, 2002, **26**, 996; (b) M. Llunel, D. Casanova, J. Cirera, J.M. Bofill, P. Alemany, S. Álvarez, M. Pinski and D. Yatumir, *SHAPE v1.1a: Program for Continuous Shape Measure Calculations of Polyhedral Xn and MLn Fragments*, 2003.
28 28 (a) G. A. Jeffrey, An Introduction to Hydrogen Bonding, Oxford University Press, Oxford, 1997; (b) T. Steiner, *Angew. Chem. Int. Ed.*, 2002, **41**, 48.
29 29 J. Loub, *Acta Crystallogr.*, 1991, **B47(4)**, 468.
30 30 V. A. Blatov and A. P. Shevchenko, D. M. Proserpio, *Cryst. Growth Des.*, 2014, **14**, 3576.
31 31 V. A. Blatov, *Crystallogr. Rev.*, 2004, **10(4)**, 249.
32 32 L. Zhou, J. Zhang, Y-Z. Lia and H-B Du, *CrystEngComm.*, 2013, **15**, 8989.
33 33 Y-H Han, C-B Tian, Q-H Lia and S-W Du, *J. Mater. Chem. C*, 2014, **2**, 8065.
34 34 (a) R. Li, X. Zhang, H. Dong, Q. Li, Z. Shuai and W. Hu, *Adv. Mater.*, 2016, **28**, 1697; (b) S. Hu, S. Li, H. Li and Y. Zhou, *J. Alloy Compd.*, 2017, **690**, 930.
35 35 E. Moreno-Calvo, T. Calvet, M. A. Cuevas-Diarte, D. Aquilano, *Cryst. Growth Des.*, 2010, **10(10)**, 4262.
36 36 F. Punzo, *Cryst. Growth Des.*, 2011, **11**, 3512.
37 37 J. Meng, Z. Liu, C. Niu, X. Xu, X. Liu, G. Zhang, X. Wang, M. Huang, Y. Yu and L. Mai, *J. Mater. Chem. A*, 2016, **4**, 4893.
38 38 C. R. Groom, I. J. Bruno, M. P. Lightfoot and S. C. Ward, *Acta Crystallogr.*, 2016, **B72**, 171.
39 39 M. Luján, F. Kubel, H. Schmid, *Z. Naturforsch.*, 1995, **50b**, 1210.
40 40 M. C. D'Antonio, A. Wladimirsky, D. Palacios, L. Coggiola, A. C. González-Baró, E. J. Baran and R. C. Mercader, *J. Braz. Chem. Soc.*, 2009, **20(3)**, 445.
41 41 A. B. P. Lever, *Inorganic Electronic Spectroscopy*; Elsevier Science Publishers B.V.: Amsterdam, Netherlands, 1984.
42 42 G. Kortum, *Reflectance Spectroscopy*, Springer, New York, 1969.
43 43 (a) D. Armentano, G. de Munno, F. Lloret, M. Julve, J. Curély, A. M. Babb and J. Y. Lu, *New J. Chem.*, 2003, **27**, 161; (b) B. Zhang; Y. Zhang, Z. Wang; ,D. Wang; ,P. J. Baker; F. L. Pratt and D. Zhu, *SCI. REP-UK*, 2014, **4**, 6451.
44 44 M. A. McGuire, *Crystals*, 2017, ***7*(5)**, 121.
45 45 S. K. Karna, Y. Zhao, R. Sankar, M. Avdeev, P. C. Tseng, C. W. Wang, G. J. Shu, K. Matan, G. Y. Guo, and F. C. Chou, *Phys. Rev.*, 2017, **B95**, 104408.

Please do not adjust margins